



Field investigation and numerical simulation of the seismic triggering mechanism of the Tahman landslide in eastern Pamir, Northwest China

Yuxuan Zhu^{1,2} · Fuchu Dai^{1,2} · Xin Yao³ · Xinbin Tu⁴ · Xinshuai Shi⁵

Received: 30 September 2018 / Accepted: 7 May 2019 / Published online: 12 May 2019
© Springer-Verlag GmbH Germany, part of Springer Nature 2019

Abstract

Landslides are one of the most common geological hazards in many parts of the world, which have brought catastrophic consequences to mankind. Seismic shaking can be an important trigger factor generally resulting in large-scale landslides. For some paleolandslides triggered by earthquakes, despite the lack of historical records, certain paleoseismic parameters can be back-analyzed. In this paper, the discrete element method (DEM) was applied to back-analyze the peak ground acceleration (PGA) triggering the Tahman landslide, a paleolandslide located in eastern Pamir, northwest China. Firstly, detailed field geological and geomorphological investigation was conducted to reveal the natural and seismic characteristics of the landslide. Subsequently, discrete element modeling was carried out. Simulation results suggested that the Tahman rock slope was stable under natural conditions. Owing to arid climate and water shortage of the study area, the influence of water was ignored. Additionally, from the perspective of the occurrence time of the landslide and geomorphologic feature of the deposits, the landslide was not caused by glacier activity and freeze–thaw events, and thus, must have been triggered by an earthquake. A peak ground acceleration (PGA) of 0.55 g was found to be a critical value for triggering landslides, and a PGA of 0.76 g could best simulate the kinematic process of a landslide when the simulation results were calibrated against the current geomorphological features of the landslide deposits. It can be concluded from the present study that: (1) PGA amplification in the rock slope was related to the topography during earthquake excitation; (2) the effective duration of the seismic wave had a considerable impact on the back-analyzed PGA, which decreased with increasing effective duration; and (3) the long runout of the Tahman landslide was due to its large volume and the interaction of the slide mass with moraines.

Keywords Paleolandslide · Earthquake · Field investigation · Discrete element modeling · PGA · Back-analysis

Introduction

Landslides are one of the most common geological disasters, especially in mountainous areas. Earthquakes have long been recognized as being major triggers of landslides, and can induce large-scale landslides, which can be catastrophic and may lead to loss of human lives or damage to property. Seismically triggered landslides are usually distributed along coseismic faults or tectonically active zones (Keefer 1984; Crozier 1992; Jibson 1996; Huang and Li 2008; Dai et al. 2011).

Earthquake-triggered landslides, in terms of occurrence age, can be divided into modern seismic landslides and paleoseismic landslides. Crozier (1992) firstly indicated that information preserved in the geologic record on the nature, distribution and age of paleoseismic landslides can be used to reconstruct regional paleoseismicity and back-analyze

✉ Yuxuan Zhu
yxzhu2017@163.com

¹ Beijing University of Technology, Beijing 100124, China
² Key Laboratory of Urban Security and Disaster Engineering, Ministry of Education, Beijing 100124, China
³ Institute of Geomechanics, Chinese Academy of Geological Sciences, Beijing 100081, China
⁴ State Grid Economic and Technological Research Institute Co. Ltd., Beijing 102209, China
⁵ Shandong University of Science and Technology, Qingdao 266590, China

certain paleoseismic parameters. Subsequently, Jibson (1996) proposed that paleoseismic landslide analysis involves three steps: (1) identifying the landslide, (2) dating the landslide and (3) showing that the landslide was triggered by seismic shaking. Later, Wechsler et al. (2009) applied Slope/W software to back-analyze the stability of a paleoseismic landslide in northern Israel, and found that high horizontal seismic acceleration ($>0.3\text{ g}$) was required to induce slope failure. Welkner et al. (2010) employed the discrete element method to back-analyze the failure mechanism of a paleoseismic landslide in the Andean Cordillera of central Chile and indicated that an M_s 7.8 earthquake would be required to trigger another rockslide from the original source area. Long et al. (2015) back-analyzed paleoseismic parameters of the Temi landslide, a large-scale paleoseismic landslide in the upper Jinsha River, China, and preliminarily concluded that the epicenter was at the Xionsong–Suwalong active fault and that the magnitude was 7.0–7.4. Therefore, it is very meaningful to study paleoseismic landslides so as to provide important reference information for the assessment of seismic risk and for designing large-scale engineering structures.

At present, numerical modeling methods of rock slope stability under seismic effects mainly include the continuum (finite element) and discontinuum (discrete element) codes. Continuum methods are generally useful for analyzing ground shock effects, but are inadequate for representing dynamic block motion, without considering dynamic or wave propagation effects. As for the jointed rock masses, the discontinuum-based discrete element codes are more appropriate than the continuum codes, because they not only allow fully dynamic analyses under plane-strain conditions, but also consider the significant influence of discontinuities on the stability of a rock slope. Dai et al. (2002) also suggested that the discrete element method is an invaluable tool for understanding the failure mechanics of landslides through back-analysis. The commercial universal discrete element code (UDEC) is considered to be an informative approach for modeling jointed rock slopes, especially when large-scale deformation and rotational movements are involved (Itasca 2004). Previous studies have demonstrated that the UDEC can effectively simulate the dynamic behaviors of jointed rock slopes. Bhasin and Kaynia (2004) assessed the stability of a 700-m-high rock slope in static and dynamic stages and estimated the potential landslide volumes. Kveldevisvik et al. (2009) analyzed the seismic stability of the Åknes rock slope in western Norway, and the dynamic input was based on earthquakes with return periods of 100 and 1000 years. Cao et al. (2011) reproduced the deformation accumulation and sliding process of the Tangjiashan rockslide triggered by the Wenchuan earthquake in 2008. Zhou et al. (2013) simulated the earthquake response and mass movement and accumulation processes of the Donghekou landslide-debris flow. However, previous studies mostly focused on analyzing stability or the

dynamic response of slopes. To our knowledge, there has been no attempt to back-analyze the PGA of a paleoseismic landslide using the UDEC.

In the present study, a detailed investigation was conducted on the Tahman landslide, a large-scale paleoseismic landslide in eastern Pamir, northwestern China (Fig. 1). The landslide is a rock avalanche owing to the landslide volume and runout (Keefer 1984). Firstly, the tectonic and geologic settings of the study area were analyzed and a brief description is provided to better understand possible seismic origins. Then a detailed field investigation was conducted for field mapping to provide geological evidence and to reconstruct the pre-failure landscape. Finally, UDEC software was then applied to back-analyze the peak ground acceleration (PGA) of the earthquake triggering the Tahman landslide and to reproduce the kinematic process of the Tahman landslide.

Regional geological and tectonic setting

The Tahman landslide is in the southwest of the Tarim Basin, south of the Muztag Ata peak, in eastern Pamir, northwestern China. Climatologically, the region is situated at the intersection of the Indian summer monsoon and mid-latitude westerlies, and has an arid climate (Seong et al. 2009). The average annual temperature is $3.6\text{ }^{\circ}\text{C}$, and the mean annual precipitation is 76 mm (Sun et al. 2006; Patar et al. 2016). Regional rock strata comprise the Paleozoic felsic gneisses, metamorphic rock (amphibolite-granulite facies) and Triassic–Lower Jurassic granite. The rock outcrops around the landslide are mainly Paleozoic felsic gneisses and Late Pleistocene moraines. A geological map of the Tahman landslide is shown in Fig. 2a. The study area is seismically active and has experienced several large earthquakes of M_s 8.0–8.9 in recent years (Fig. 1b). This is evidenced by the surface rupture and fault scarp being extensively distributed in the study area.

As shown in Fig. 1b, tectonic activity is intensive in the study area, and the Kongur Shan extensional system is the main active deformation in the eastern Pamir (Arnaud et al. 1993; Brunel et al. 1994; Robinson et al. 2004, 2007). It is about 250 km long, generally striking NW–SE and dipping to the W. From north to south, this extensional system comprises the Muji fault, the Kongur Shan normal fault, the Tahman normal fault and the Tashkorgan normal fault. The northernmost is the 60-km-long and S–SW-dipping Muji fault. At the eastern terminus of the Muji fault, the strike changes abruptly from W–NW to N, connecting with the Kongur Shan normal fault. The Kongur Shan normal fault is generally N-striking, continuing for about 20 km south of the Tagamansu Valley and terminating at the Tashkorgan River. The Tahman normal fault is about 20 km long, dipping steeply to the W–NW. As a transformation fault, it links the north to the Kongur Shan normal fault and the south to the Tashkorgan normal fault

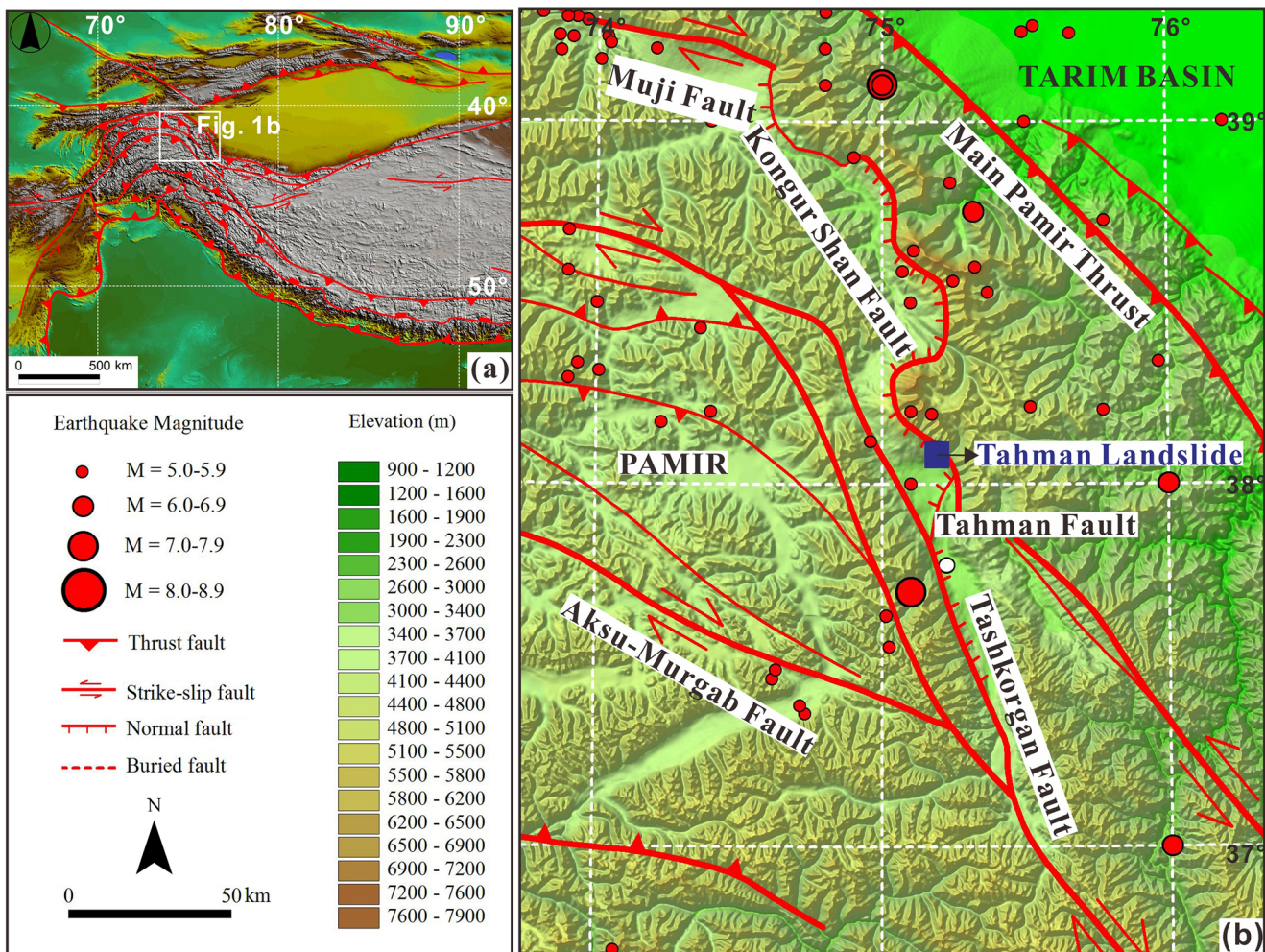


Fig. 1 Location and tectonic setting of the study area: **a** location of the study area (white dashed box showing **b**); **b** Shuttle Radar Topography Mission (SRTM) color-shaded relief map showing the location of the Tahman landslide, historic earthquakes and the major faults in the study area

(Robinson et al. 2004). The Tashkorgan normal fault is about 75 km long at the southernmost part of the Kongur Shan extensional system. This fault strikes N to N–NW and dips steeply to the E.

Methods

Field mapping

A field investigation was conducted in August 2016 to identify the characteristics of the Tahman landslide and collect some fundamental data for numerical modeling. The 1:50,000 digital geological map was used to locate the faults and to identify the lithological features of the bedrock. Parameters including slope angle, deposit thickness and area, and initial landslide volume were obtained from a digital topographic map and field measurements using GIS.

Numerical simulations

The commercial UDEC software was used for back-analysis in the present study, and the dynamic calculation was conducted after the static calculation. To simulate the earthquake trigger, a simplified harmonic sinusoidal wave was applied to the base of the UDEC model as input excitation:

$$V = V_{\max} \cdot \sin(2 \cdot \pi \cdot f \cdot t) \quad (1)$$

where V_{\max} is the peak ground velocity in m/s, f is the dominant frequency in the study area in Hz, and t is the effective duration in second. The peak particle velocity, V_{\max} , is calculated as follows:

$$V_{\max} = PGA / (2 \cdot \pi \cdot f) \quad (2)$$

where PGA is the peak ground acceleration. Then the PGA can be back-analyzed by adjusting the value of V_{\max} .

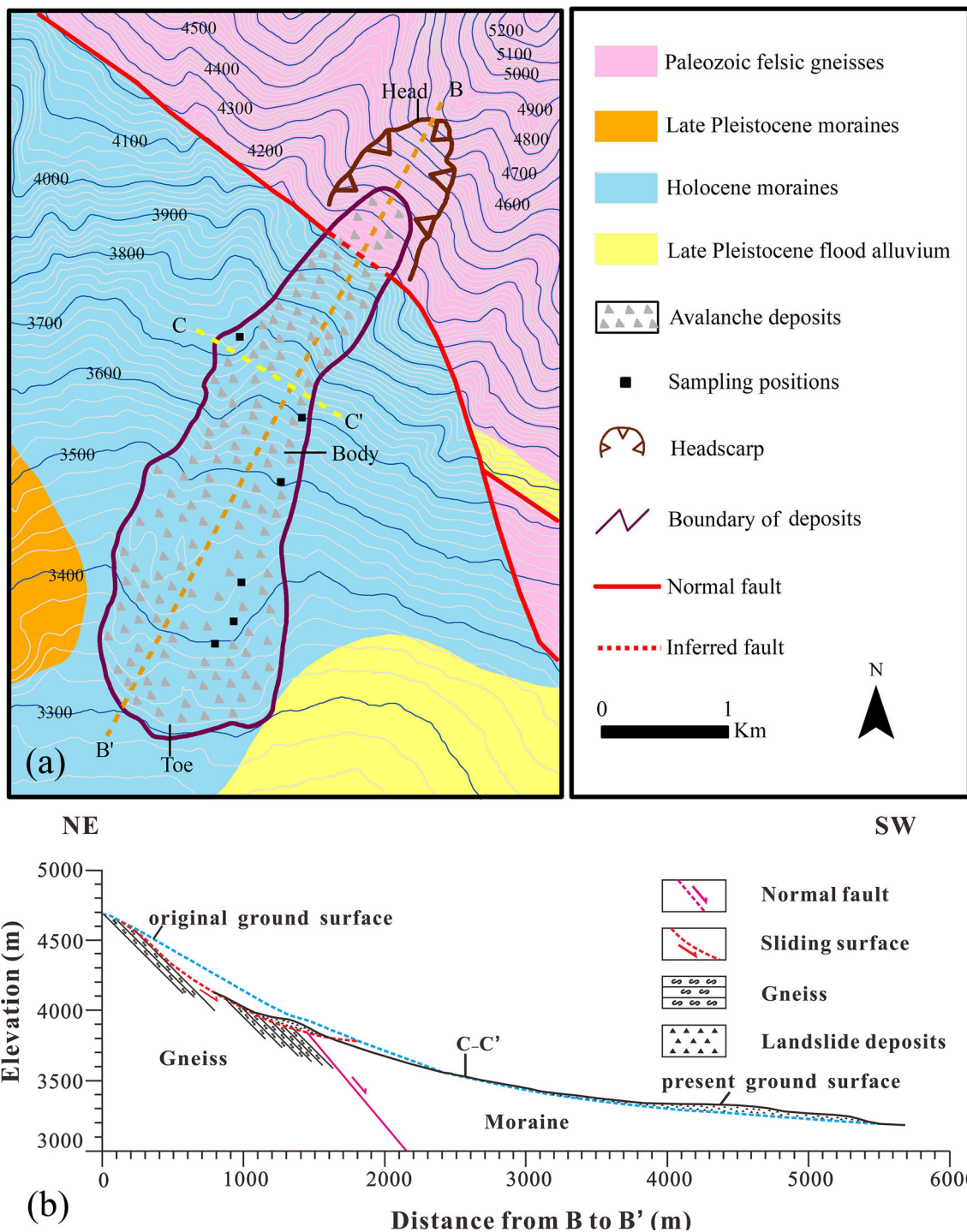


Fig. 2 Geological condition of the landslide: **a** 1:50,000 geological map of the Tahman landslide, where the brown dashed line (B–B') denotes the main section line for numerical modeling, the yellow dashed line (C–C')

denotes the section line for velocity estimation, and the black boxes are the sampling positions by Yuan et al. (2012); **b** cross-section B–B' in (a) showing reconstructed pre-failure topography and geology

According to GB 18306 (2015), the dominant frequency in the study area is 2.2 Hz, which agrees with the observation of Bhasin and Kaynia (2004) that the dominant frequencies at rock slope sites are normally in the range of 2–5 Hz. The effective duration was determined using the following equation proposed by Bommer and Martinez (1999):

$$\text{Log}(D_E) = 0.69 \cdot M_w - 3.7 \quad (3)$$

where M_w is the earthquake magnitude ranging from 5.0 to 8.0. Therefore, the effective duration (DE) is 0.6–66 s. And the average DE of 35 s was adopted in the section “Discrete element modeling”. Following the guidelines of Itasca (2004),

the critical damping was set to a small value, 0.005, in the present study.

Characteristics of the Tahman landslide

General characteristics

The panoramic satellite image of the Tahman landslide was taken from Google Earth (Fig. 3). Field investigation revealed that the elevation difference between the highest and the furthest point of the landslide is about 1500 m. The maximum runout is about 5420 m horizontally with an equivalent friction coefficient of about 0.28. As shown in Fig. 2a, the landslide track was curved instead of straight. Initially, the landslide mass was dislodged from the source area and moved SW. However, the avalanche debris turns 10° to the south at about 2.43 km from the source because of an obstruction in the terrain to the west of the mountain. The difference in height between the deposits at two sides can be observed in cross-section C–C' (Fig. 4b). It is apparent that the deposits on the

right side are 74 m higher than the deposits on the left side. Therefore, the velocity of the sliding materials at this position is estimated to be about 50 m/s using the following superelevation-based equation, where superelevation is defined as the elevation difference in a channelized deposit inside and outside of a curve (Hungri et al. 1984; Boulton et al. 2006; Dai et al. 2011):

$$V = (r \cdot g \cdot \tan \theta \cdot \cos \alpha)^{0.5} \quad (4)$$

where g is the gravitational acceleration, r is the radius of curvature in meters, θ is the transverse slope, and α is the longitudinal slope. This equation was developed based on the assumption that the gravitational force balances the centrifugal force that causes a flow to climb the outside wall of a curved channel. The parameters used in Eq. (4) are shown in Fig. 4. Additionally, the wave-like features of the deposits at the landslide toe also indicated that the landslide had moved rapidly (Fig. 3).

The field investigation showed that both sides of the landslide body were deeply eroded by the gullies, and the

Fig. 3 Aerial photograph showing a panoramic view of the Tahman landslide (map produced with the kind permission of Google Earth)

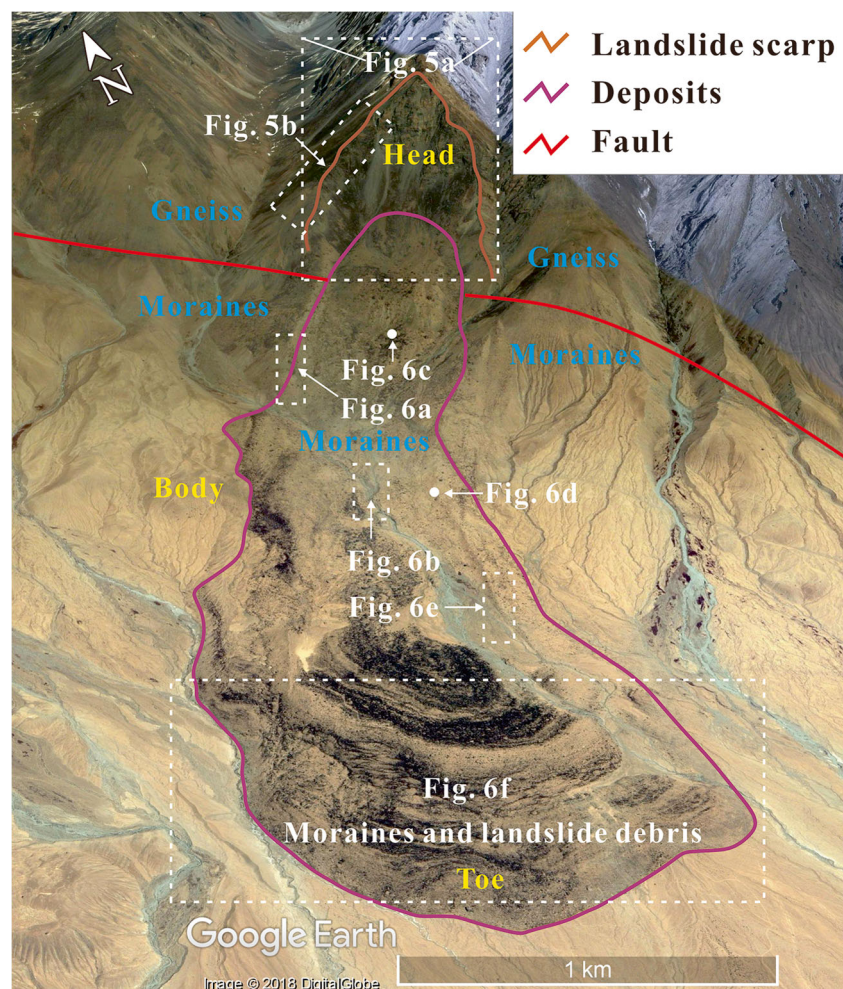
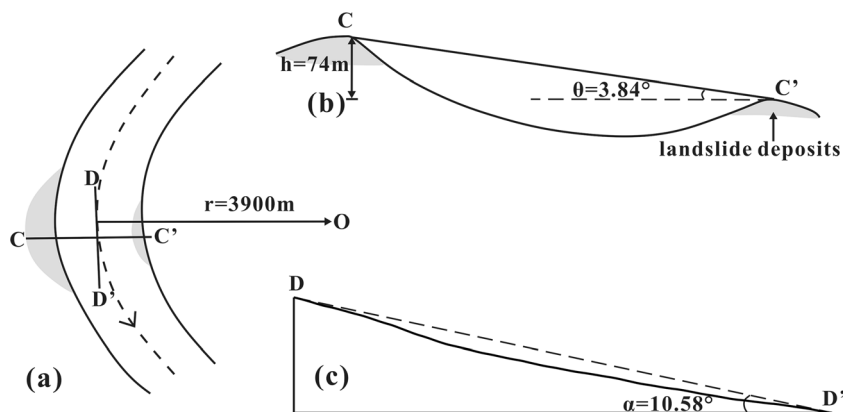


Fig. 4 Schematic diagram showing the superelevation of the avalanche debris: **a** plan view; **b** cross-section C–C' (transverse direction); **c** cross-section D–D' (longitudinal direction). Location of cross-section C–C' is shown in Fig. 2



thickness of accumulated rock varnish reached 2–5 mm. It was difficult to determine the exact occurrence time of the Tahman landslide due to the lack of historical documents and aerial photographs. To estimate the landslide occurrence time, six gneiss boulders were collected from the slope surface for ^{10}Be exposure dating by Yuan et al. (2012). The sampling points are shown in Fig. 2a. The ^{10}Be dating results indicate that the landslide occurred 6.8 ± 0.2 ka B.P., and therefore can be classified as a paleolandslide.

Characteristics of the source area

The source area was a ridge at elevation (EL) 3900–4800 m before landsliding. Initial failure involved a rock slope angled at $27\text{--}29^\circ$, forming a chair-shaped topographic feature and a steep backscarp with a slope angle of $\sim 42^\circ$ (Fig. 5a). The 1:50,000 geological map (Fig. 2a) shows that the source rock was mainly composed of Paleozoic felsic gneiss, with a foliation plane dipping $50\text{--}60^\circ$ to the SW. The landslide scarp was steep, rugged and almost parallel with the foliation plane, above which was a steep slope covered by snow. Two sets of dominant discontinuities were observed: a persistent bedding plane (JS1) with spacing of 1–5 m parallel to the slope, and a persistent cross-cutting joint set (JS2) with spacing of 5–15 m and dipping $60\text{--}65^\circ$ into the slope (Fig. 5b). In addition,

two sets of subordinate discontinuities were observed: a non-persistent joint set (JS3) with spacing of 4–5 m and dipping $85\text{--}90^\circ$ away from the slope, and a non-persistent joint set (JS4) with spacing of 5–8 m and dipping 65° away from the slope. At about EL 4012 m, the landslide was traversed by the Kongur Shan normal fault. The hanging wall was mainly composed of moraines (Figs. 2a and 3). It could be speculated from some of the remaining moraine outcrops that many moraines were scraped and entrained by gneiss fragments during the landslide.

Characteristics of the deposits

The deposits were generally distributed from EL 3290 to 4230 m in an area of about 4.6×10^6 m², estimated using Google Earth, and with an average height of 25 m as estimated by digital elevation model (DEM) and field observation. Thus, the volume of the deposits was approximately 115×10^6 m³. A 25% volume increase was assumed based on the fragmentation of the detached mass and entrainment during transport (Hung and Evans 2004). The pre-failure volume of the Tahman landslide was then estimated to be about 92×10^6 m³.

The field survey found that the deposits were generally tongue-shaped like a lava flow, and walking on the surface of deposits was very difficult because of the scattered large

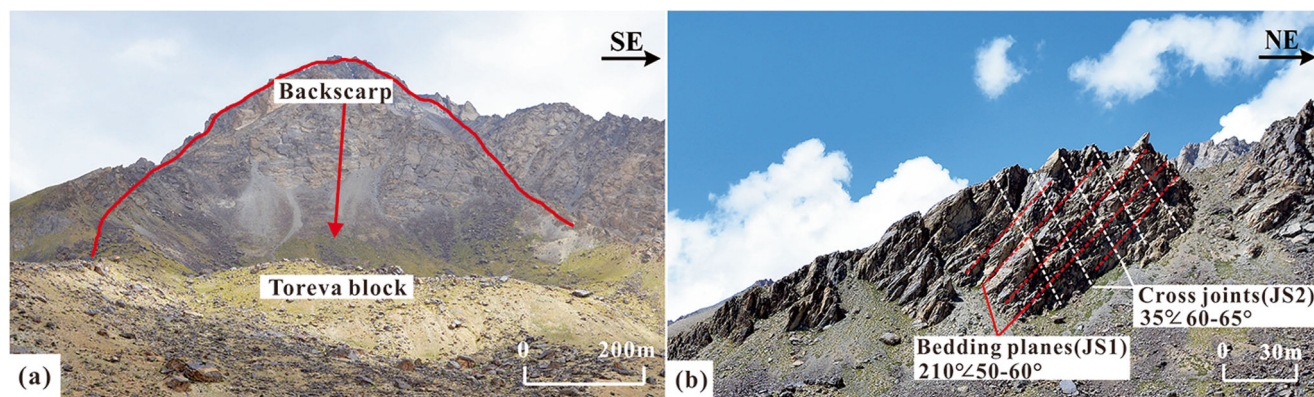


Fig. 5 Photographs of source area and the two dominant joint sets: **a** Backscarp and Toreva block; **b** bedding plane and cross joint

blocks. The top of the deposit was a Toreva block (Fig. 5a), with an elevation ranging from EL 3900 to 4060 m. Its top surface was a gently sloping platform about 560 m long and about 150 m wide, and its downward escarpment was up to 130 m with a 45° slope angle. The materials in this part were mainly colluvial deposits and moraines. The exposed moraines indicate that some materials were entrained and scraped during avalanche debris transportation (Fig. 6a and b). Grain-size distribution was continuous across a broad range, from fine-grained soil-like materials to well-rounded moraine to

angular gneiss blocks. Some individual large blocks measured more than 16 m in this part (Fig. 6c).

The middle of the deposits was the thinnest of the three parts with an average thickness of 10 m. Interestingly, a gneiss boulder with a diameter of 3 m was inserted into the ground and covered by soil and gravel of 5–30 cm diameter (Fig. 6d). It was evidently not made by humans. It is likely that the large-size boulder stopped moving first because it ran out of momentum, but the soil and gravel continued moving and climbing up on the surface of the boulder, with some

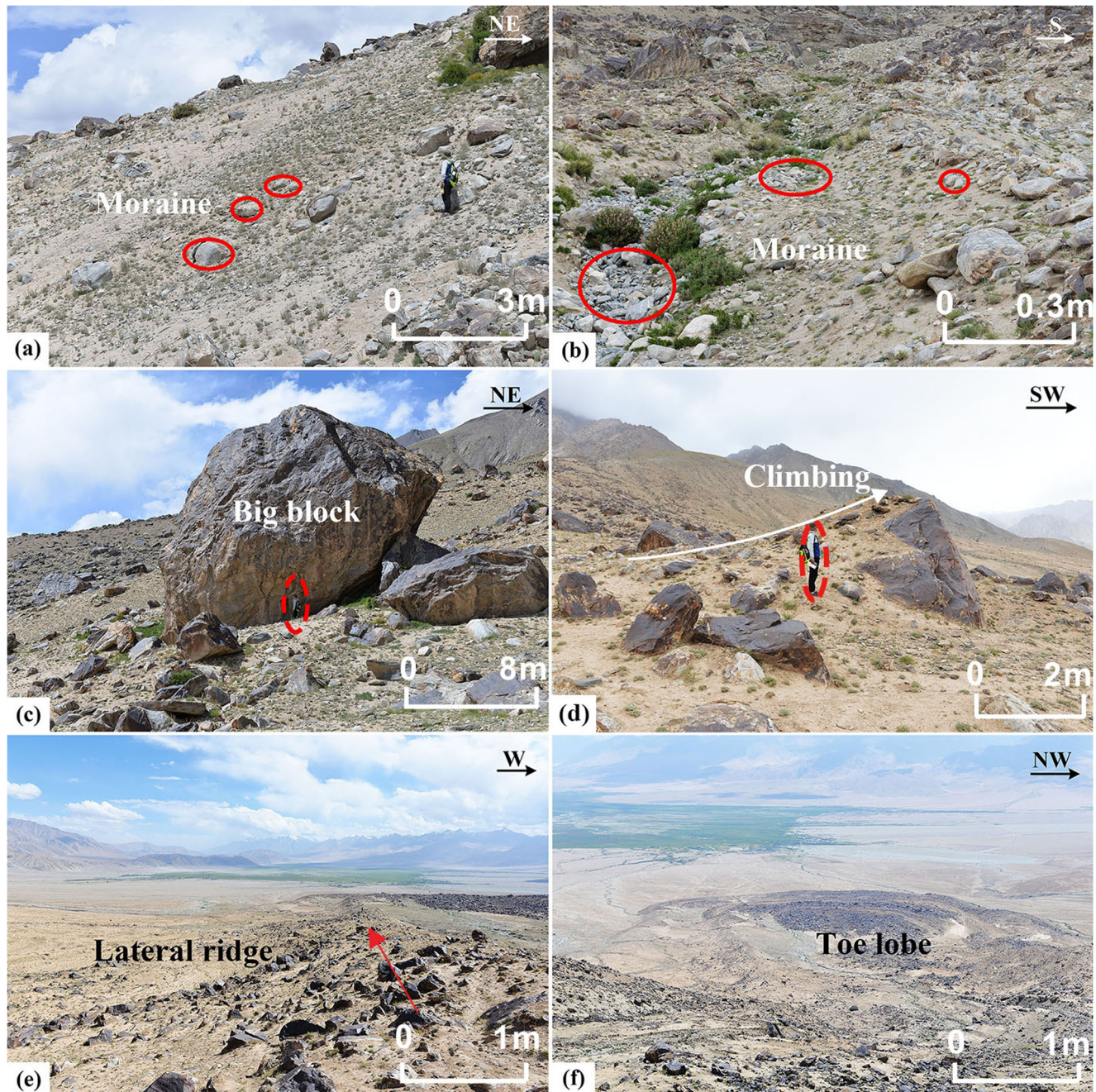
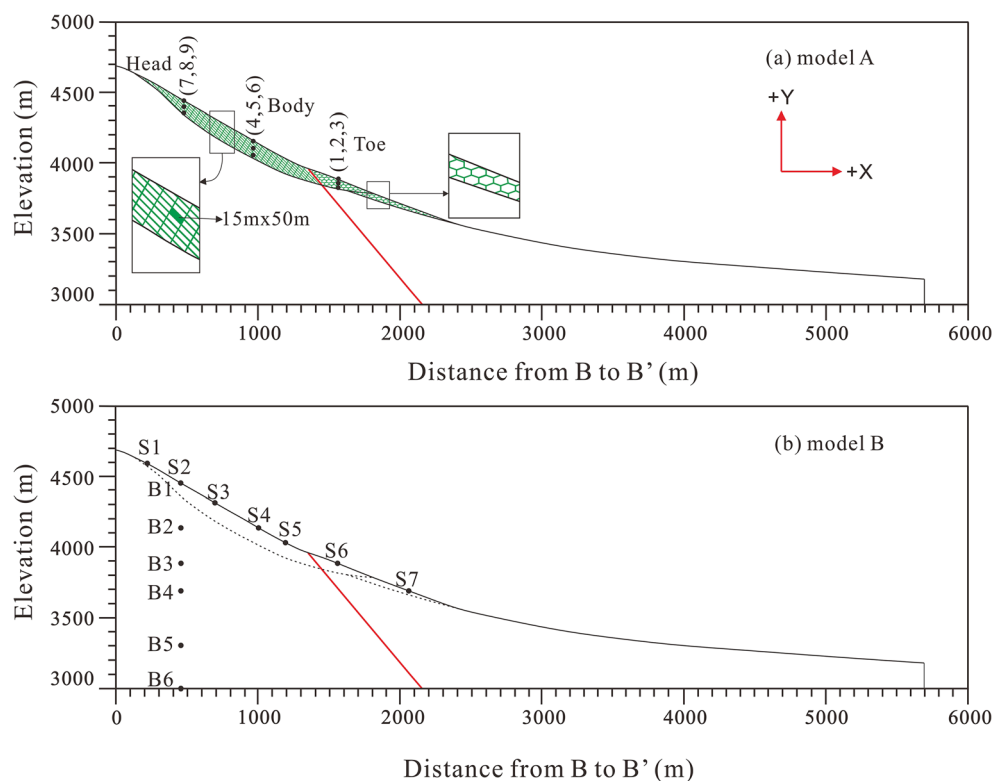


Fig. 6 The deposits of Tahman landslide: **a** the outcrop of remaining moraines in the west margin of the slide mass; **b** the scraped moraines in the middle of the landslide; **c** large block at the top of the deposits; **d** the phenomenon of “hill climbing”; **e** left lateral ridge; **f** toe lobe

Fig. 7 Numerical models and monitoring points: **a** model A for simulation of the mass movement and accumulated process; **b** model B for analysis of the seismic response



accumulating on the surface of the boulder and some crossing the boulder and landing on the ground. In addition, well-defined lateral ridges formed during the landslide, as shown in Fig. 6e.

At the toe of the landslide deposit, a toe lobe was observed in the field, which reflected the fluidization characteristic of the landslide (Fig. 6f). Materials comprised angular gneiss boulders from the source area and entrained moraines during landsliding. The average thickness of deposits in this part is about 37 m. The distal rim at the leading edge of the landslide toe was several meters higher than the immediate surroundings, and looked like a low earth dam when observed from a certain distance.

Speculation of triggering mechanism

Owing to the lack of historical documentation, the formation mechanism of landslides is uncertain. Based on the geological and tectonic settings in the study area and the detailed field

investigation, we consider that the Tahman landslide was most likely induced by a paleoseismic event. There are various reasons for this. First, large-scale and long runout landslides are generally considered to have been triggered by earthquakes or rainstorms (Tsou et al. 2011). However, according to Patar et al. (2016), the mean annual rainfall in this region is 76 mm. It is obvious that the annual rainfall is very low in this region because of the arid climate (Sun et al. 2006). Therefore, heavy rainfall is an unlikely explanation. Second, tectonic activity was intensive, and there were many large-scale rock landslides spatially clustered around the fault zones in this region. In addition, ancient earthquakes were frequent in this area (Fig. 2a). Seong et al. (2009), based on a systematic investigation, also considered that major rockslides or avalanches (including the landslide under study) in this area were triggered by earthquakes. Finally, Seong et al. (2009) reported two glacial events (Karasu and Subaxh) in our study area, aged from 151 to 367 ka and 53–67 ka, respectively. However, the ^{10}Be dating results revealed that the landslide

Table 1 Physical and mechanical parameters of rock mass used in the UDEC models

| Lithology | Density (kg/m ³) | Young's modulus (GPa) | Poisson's ratio (–) | Cohesion (MPa) | Friction (°) |
|----------------------------|------------------------------|-----------------------|---------------------|----------------|--------------|
| Gneiss (in the slide mass) | 2700 | 25 | 0.25 | 7 | 48 |
| Gneiss (in the slide bed) | 2700 | 35 | 0.22 | 9 | 51 |
| Moraine | 2200 | 3 | 0.28 | 0.109 | 30 |

Table 2 Mechanical parameters of structural planes used in the UDEC models

| Categories | Normal stiffness (GPa/m) | Shear stiffness (GPa/m) | Cohesion (MPa) | Friction (°) |
|----------------|--------------------------|-------------------------|----------------|--------------|
| Bedding planes | 2 | 1 | 0.4 | 32 |
| Joints | 2 | 1 | 0.1 | 35 |

occurred 6.8 ± 0.2 ka B.P., which suggests that this landslide was not connected to these glacier events. In addition, it is also evident from the geomorphologic features of the deposits that the landslide was not caused by freeze–thaw events, because no evidence of periglaciation was found in the deposits, while the backscarp was rough, and the rock masses in the source area were intensely fractured, which are typical features of a source area for an earthquake-triggered landslide (Jibson 1996). Therefore, we conclude that this landslide was the result of an ancient seismic event.

As described by Evans et al. (2006), the mode of initial failure in bedrock slopes is strongly controlled by slope geometry and geologic structure. For the Tahman landslide, when the earthquake occurred, the top of the slope experienced high acceleration due to topographical amplification and then failed along the bedding planes. Along with earthquake excitation, the deformation extended to the toe of the slope, leading to the formation of shear fractures. When the top of the tensile fractures connected with the toe of the shear fractures, the sliding surface was formed, and the slope slid along the sliding surface. The field investigations showed that the upper sliding surface was deep and almost parallel with the bedding plane, and the lower sliding surface was only slightly inclined, which was consistent with the failure mode. Given the prehistoric nature of the slide, the exact pre-failure geometry remains unclear. However, the geometry was reconstructed based on the 1:50,000 geological map and our field data, as shown in Fig. 2b.

Discrete element modeling

Numerical models

To more directly verify the likelihood of seismic or aseismic triggering of the Tahman landslide, numerical modeling was conducted in this section. As shown in Fig. 7, two pre-failure slope models (model A and model B) were established. The simplified and idealized 2D discrete element models were developed according to the topographic and geological cross section taken along the main sliding direction (B–B' in Fig. 2b). Model A was used to simulate the mass movement and accumulation process. According to our field data, two dominant joint sets (JS1 and JS2) with average joint spacing of 3 m and 10 m, respectively, were considered in the slide mass. The joint spacings were increased five-fold to improve

computational efficiency. Therefore, the average block size of the sliding mass was $15 \text{ m} \times 50 \text{ m}$. The Voronoi blocks under the sliding mass were used to simulate the moraines to investigate entrainment during landslide propagation (Fig. 7a).

In model A, the slide bed was treated as deformable material, and the slide mass was treated as a rigid material because of its negligible deformation compared with its runout. The Mohr–Coulomb criterion was used for the deformable materials, and the Coulomb slip criterion was used for all structural planes. Model B was established to analyze the seismic responses of the slope whilst limiting the influence of the joints as much as possible. In this model, both the slide mass and the slide bed were treated as continuous deformable materials, and the Mohr–Coulomb criterion was used for the material model of the rock mass.

Determination of mechanical parameters

Rock mass characteristics were assessed using a modified geological strength index (GSI) (Sonmez and Ulusay 1999). The GSI values of the gneiss obtained from field estimation ranged from 75 to 80. Referring to the China Institute of Water Resources and Hydropower Research (1991), the uniaxial compressive strength of the intact rock ranges from 80 to 110 MPa, and Young's modulus ranges from 30 to 40 GPa. Our field observations showed that the rock masses were weakly to moderately weathered in the slide mass and fresh in the slide bed. Therefore, the lower value was used for the slide mass and the higher value was used for the slide bed. The strength parameters of the rock mass were calculated using the generalized Hoek–Brown failure criterion (Hoek and Brown 1997). The parameters used for the moraine and structural planes followed those of previous studies (Yuan et al. 2009; Zhou et al. 2013) and empirical judgment. The material parameters used in the simulation are listed in Tables 1 and 2.

Boundary conditions

The boundary conditions for static and dynamic analyses are different. For the static analysis, the lateral sides of the model were fixed in the X direction, and the base was fixed in the Y direction (Bhasin and Kaynia 2004). The dynamic analysis was performed after the static analysis. Free-field conditions were used for the lateral boundaries, and the bottom boundary was changed to a viscous boundary, which is non-reflecting

and can absorb waves reflected from the slope. In the UDEC simulation, the dynamic load in the form of the velocity curve could not be added directly to the viscous boundary; instead, the load had to be transformed to a stress curve. The excitation was applied to the base of the model in the form of shear stress, as specified by Itasca (2004):

$$\tau = 2(\rho \cdot V_s) \cdot V_{\max} \quad (5)$$

$$V_s = (G/\rho)^{0.5} \quad (6)$$

where τ is the shear stress, ρ is the rock mass density, V_s is the shear wave velocity propagating through the rock mass, V_{\max} was defined in Eq. (2), and G is the shear modulus. The shear stress calculated from Eq. (5) was doubled to compensate for the viscous boundary.

Simulation results under static condition

The results of the static analysis indicated that the slope was in equilibrium under natural conditions. Figure 8 illustrates horizontal displacement over time for the monitored points (1, 4, 7) and indicates that the slope was in equilibrium in model A (Fig. 7a). This stage is considered to represent the existing in-situ stage, in which the rock mass conditions are stable (Bhasin and Kaynia 2004). Owing to the arid climate and water shortage in the study area, the influence of water can be ignored. Furthermore, considering the estimated occurrence time of the landslide and geomorphologic features of the deposits, the landslide was not caused by glacier activity. Therefore, the landslide must have been caused by the ground shaking during an earthquake.

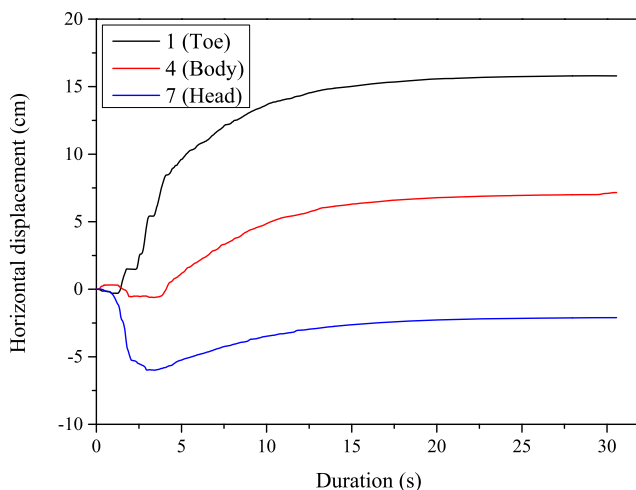


Fig. 8 The displacement of monitored points (points 1, 4, 7) in the X direction indicating equilibrium conditions

Simulation results under dynamic conditions

Kinematic process of slide mass

After several trials of dynamic analysis using model B (Fig. 7b), it was found that the PGA of 0.55 g was a critical value to trigger a landslide. In other words, when the PGA was less than 0.55 g, the rock slope was stable and no landsliding occurred. That is, the landslide has difficulty sliding under other external conditions. To represent the failure process of the Tahman landslide, PGA was gradually increased to 0.76 g, and a best-fitting simulation result was obtained by calibrating the simulation results to the current geomorphological features of the deposits (Figs. 2a and 9h). The actual landslide deposit area was slightly different to that represented in the model owing to the influence of local microtopography, which could not be reflected in the simulation.

Figure 9 presents the landsliding process in a short time interval obtained by dynamic modeling. The landsliding process can be divided into three stages, namely deformation, sliding and accumulation. When dynamic excitation lasts for 10 s, the top of the slope becomes loose and tensile cracks form (Fig. 9a), but the relative location of most blocks remains unchanged. Thus, the process from 0 to 10 s can be considered to be the deformation stage.

As shown in Fig. 9b, sharp sliding took place at the head of the slide mass at about 25 s. From 10 to 110 s, the slide mass experienced a sliding stage in which the slide mass disintegrated into fragments, which was due to collisions and fragmented rock blocks sliding rapidly along the steep terrain of the slope. After about 110 s, the slide mass gradually stopped and finally deposited on the gentle slope surface.

Variation in velocity during landsliding

As shown in Figs. 10 and 11, velocity along the X (horizontal) and Y (vertical) directions were recorded to interpret the kinematic process of the slide mass.

In the X direction (Fig. 10), the velocity of the toe of the slide mass initially increased rapidly owing to a lack of obstructions. At about 37 s, the velocity reached the peak value (about 28 m/s). Subsequently, the collisions and interactions in the toe of the slide mass caused temporary deceleration. However, secondary acceleration occurred in the slide mass toe (at about 60 s) as a result of pushing from blocks behind, and the peak velocity was about 52 m/s. Finally, this part stopped moving at about 150 s. As for the body of the slide mass, the velocity was stable with few fluctuations before 20 s. After 20 s, the velocity fluctuated intensively, especially for surface blocks, and reached the peak value (55 m/s) at about 70 s. After these intense fluctuations, the velocity decreased gradually until movement stopped. As for the head of the slide mass, the velocity was relatively low before 60 s as a

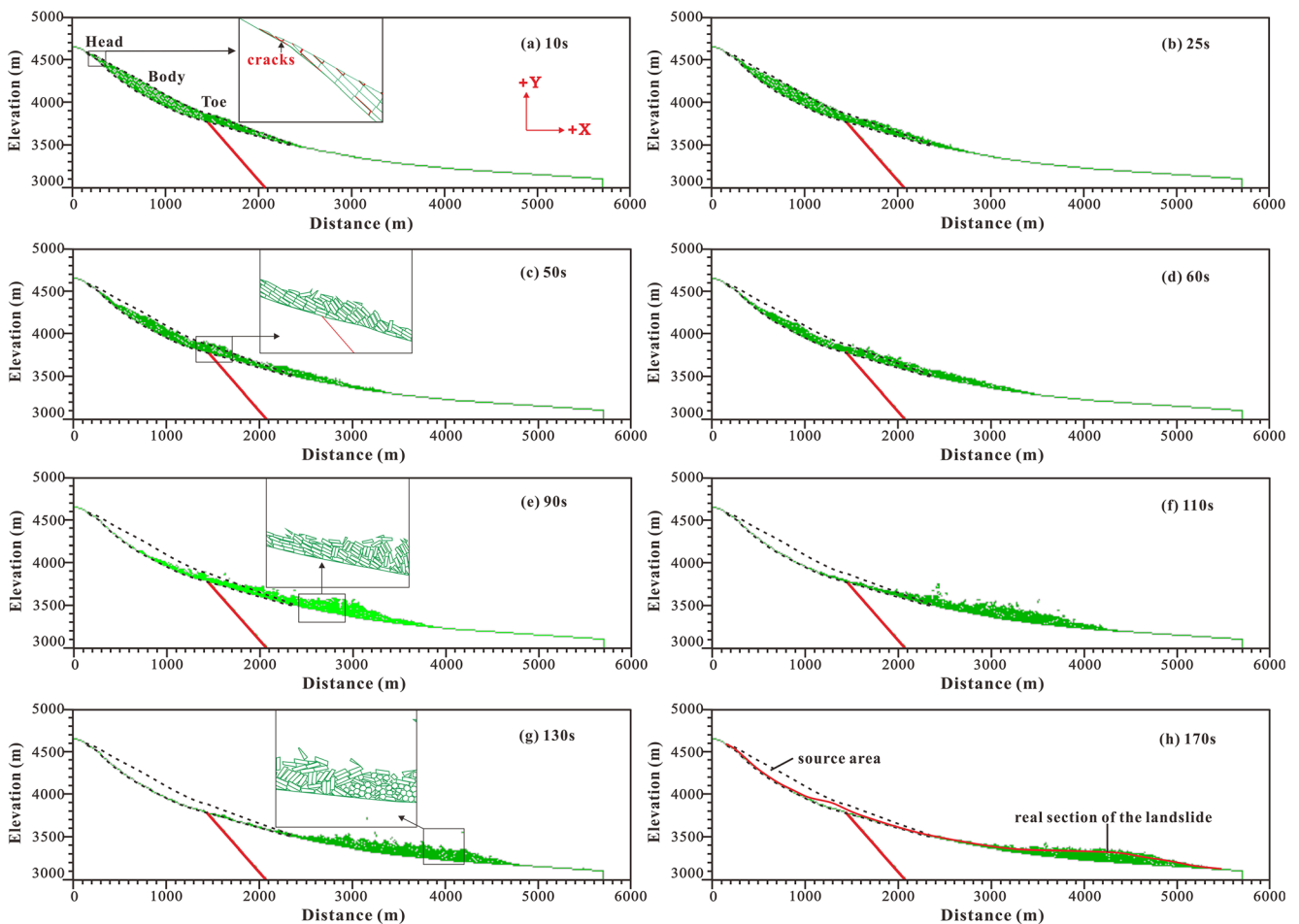


Fig. 9 Landsliding process obtained by dynamic modeling: **a** 10 s; **b** 25 s; **c** 50 s; **d** 60 s; **e** 90 s; **f** 110 s; **g** 130 s; **h** 170 s

result of obstruction from the body of the slide mass. After about 60 s, the velocity rapidly increased and reached the peak value (about 46 m/s) at about 90 s. Then the velocity quickly decreased, reaching zero at about 160 s. The maximum velocity was consistent with the estimation in the section “General characteristics”, which indirectly verifies the rationality of the numerical simulation.

In the Y direction (Fig. 11), negative velocity indicates the downslope motion of the slide mass, while positive velocity indicates the upward motion (bounce behavior) of the slide mass (Lo et al. 2011). It is obvious that the velocity was mostly negative, which implies that the landslide had a steep terrain leading to significant downward motion of the slide mass. The velocity curve of the slide mass toe was hump-like, and the peak velocity was about 23 m/s. As for the body of the slide mass, the velocity fluctuated intensively, which indicates a strong collision between the blocks. The velocity reached the peak value (50 m/s) at about 90 s. As for the head of the slide mass, the velocity of the blocks close to the slope surface (point 7) fluctuated more intensively than that of the blocks inside the slope (points 8 and 9), which indicates that blocks near the surface experience vertical ‘jumping’ during the sliding process due to seismic loading.

The velocity in this part reached peak value (about 36 m/s) at 98 s. In general, the whole trend of velocity variations in the Y direction was similar to that of the X direction.

PGA amplification related to topography

Wave amplification is a common phenomenon, which has been investigated in detail by many researchers (Harp and Jibson 2002; Havenith et al. 2003a, b; Meunier et al. 2007, 2008; Gaudio and Wasowski 2011; Wolter et al. 2016). Strong ground motion and topographic amplification of a slope were emphasized as causes of rock avalanches during earthquakes (Huang 2009; Yin et al. 2009). Therefore, to investigate PGA amplification related to the topography of the Tahman landslide, two sets of monitoring points were set in model B (Fig. 7b). The point B6 was used to normalize the amplification coefficient, because the point B6 was at considerable depth within the bedrock (3000 m, model base), and this was an arbitrary amplification coefficient devised to indicate the relative difference of the amplification at the other reference points (B1–B5 and S1–S7). As shown in Fig. 12a, the horizontal PGA amplification coefficients tended to increase with

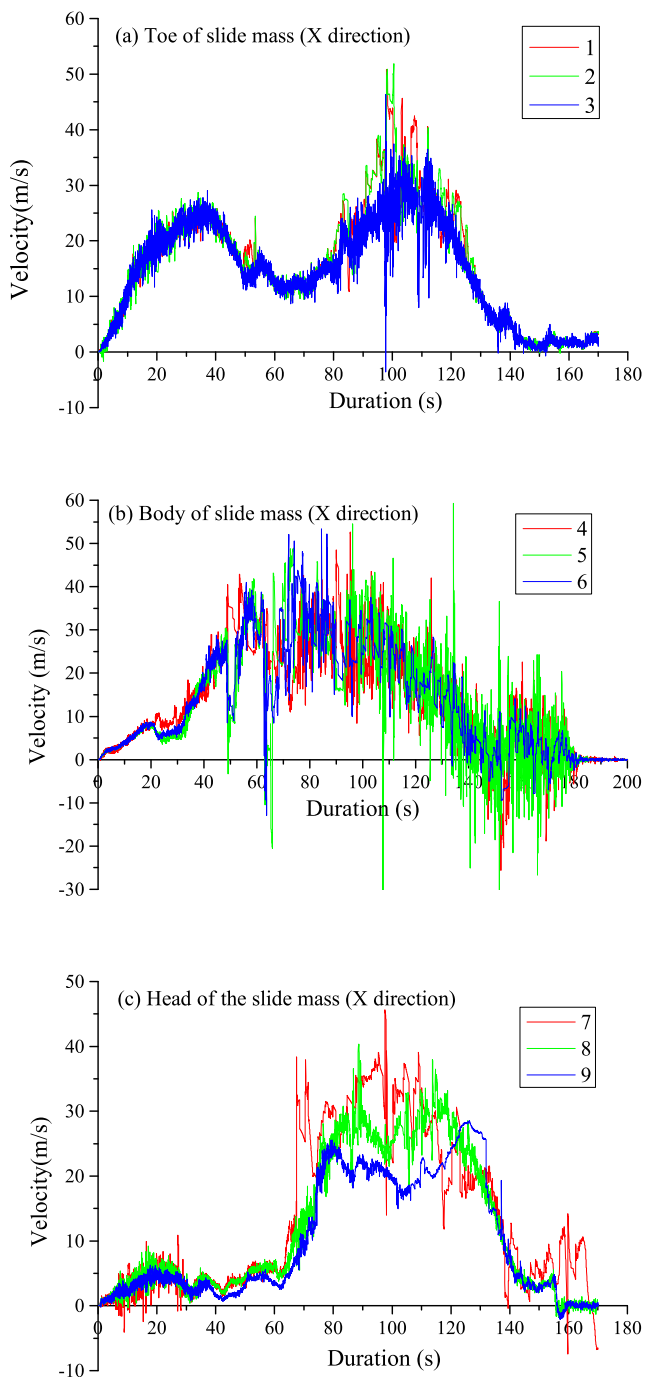


Fig. 10 Velocity in the X direction during landsliding: **a** toe of the slide mass; **b** body of the slide mass; **c** head of the slide mass

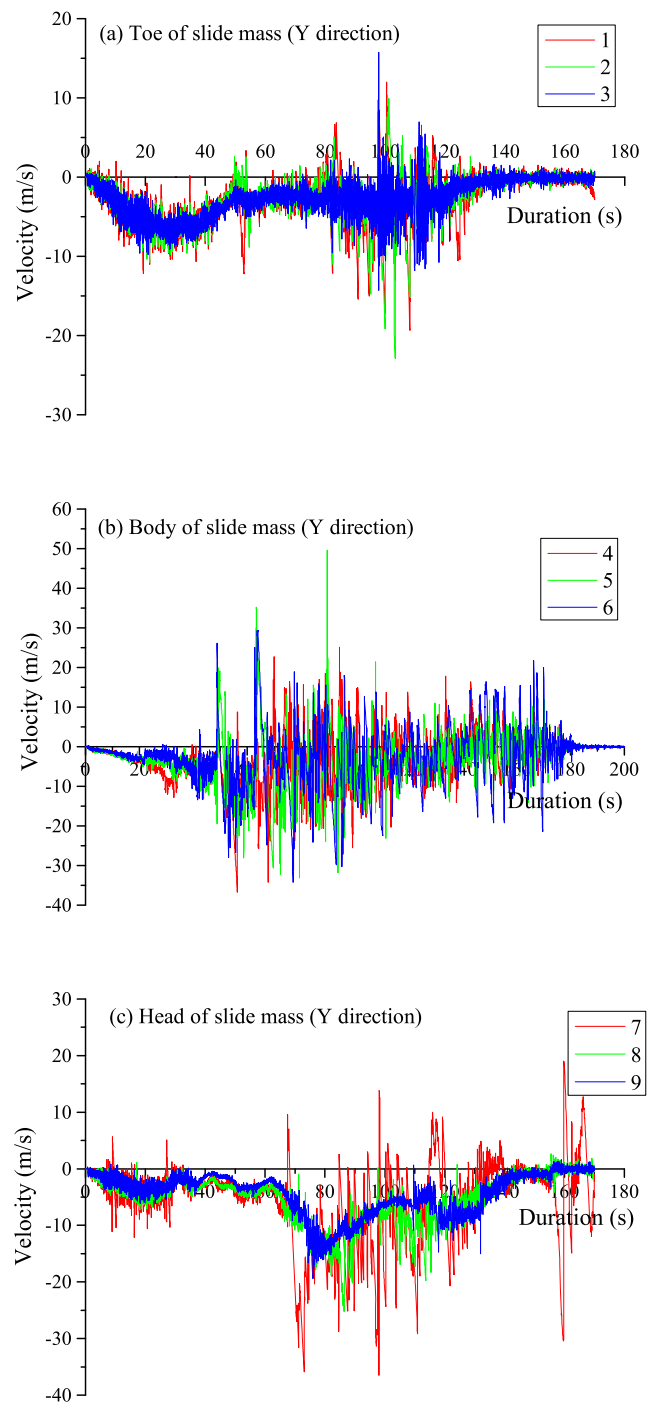


Fig. 11 Velocity in the Y direction during landsliding: **a** toe of the slide mass; **b** body of the slide mass; **c** head of the slide mass

elevation both on the slope surface and inside the slope, and PGA was most amplified at the top of the slope. This also suggested that at the beginning of the earthquake, slope failure began at the top. In addition, by comparing the horizontal PGA amplification coefficients of three sets of points S4–B2 (Fig. 12b), S6–B3 and S7–B4 at the same elevation, the mass acceleration at the slope surface was found to be higher than that inside the slope.

Discussion

Influence of effective duration on PGA back-analysis

Parameters related to earthquake motion include the amplitude and duration of seismic shaking and the seismic spectrum. Commonly, seismic response is strongly dependent upon not only the amplitude, but also the duration of seismic shaking.

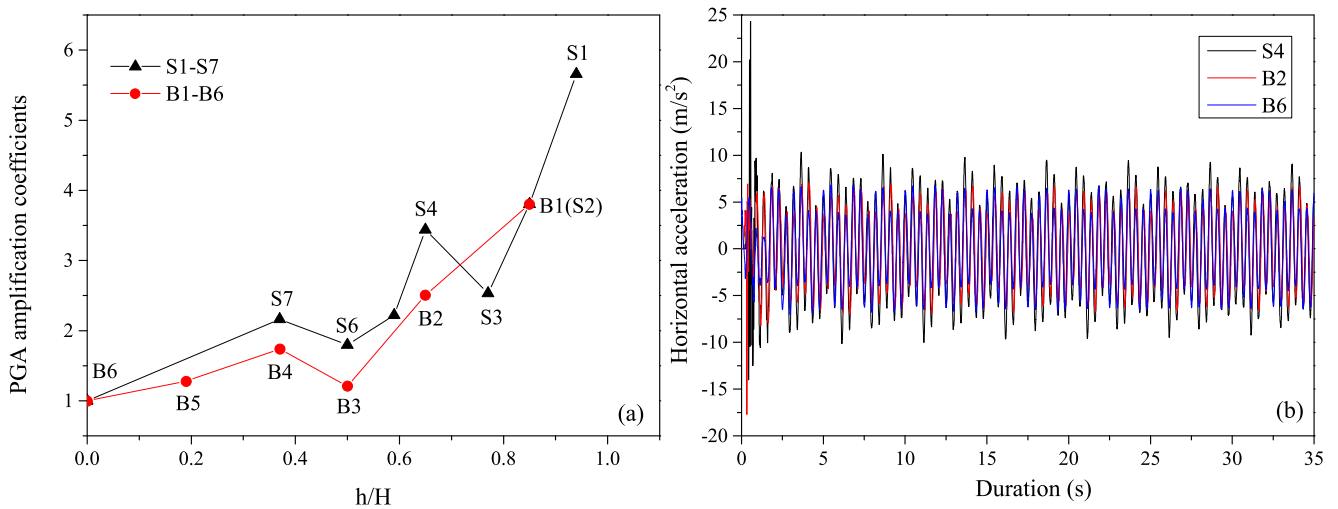


Fig. 12 Peak ground acceleration (PGA) amplification of the rock slope: **a** the PGA amplification coefficients in profiles S1–S7 and B1–B6, where h is the height difference from the monitoring points to the model base,

and H is the total height difference of the landslide; **b** time-history of the horizontal acceleration for the monitoring points S4, B2 and B6

When peak acceleration is constant, higher magnitude means longer duration of the earthquake (Bommer and Martinez 1999; Welkner et al. 2010). Therefore, different durations should be used for dynamic simulation to study their effect on the PGA back-analysis. According to Eq. (3), the effective duration varying from 15 to 55 s was used in the present study (Table 3). The results indicate that PGA decreases with increasing duration. As for the critical PGA, for the shortest duration (15 s), a PGA of 0.63 g is required to trigger sliding, but for the longest duration (55 s), a PGA of 0.53 g is sufficient to trigger sliding.

Mobility of the long-runout Tahman landslide

Previous studies have attributed the long runout of landslides to the presence of a fluidizing medium such as air, water, vapor or volcanic gases. However, for the present study, no relevant evidence could be found in the field. Comparison with other subaerial, non-volcanic landslides suggests that a plot of runout distance versus landslide volume results in a stronger correlation (Fig. 13). This result is in accordance with that of Davies (1982) and Legros et al. (2000). Similarly, other researchers (Scheidegger 1973; Corominas 1996) have found

a linear correlation between landslide volume and angle of reach, which clearly suggests that the angle of reach decreases with increasing landslide volume.

In addition, the moraines are well-developed in this landslide. To investigate the influence of moraines on the moving distance of landslide debris, we simulated two scenarios, one with and one without moraines. The results showed that the presence of moraines is conducive to long distances of landslide movement (Fig. 14). This can be explained by the roundness of the moraines reducing the friction of the landslide debris during movement and increasing the runout distance. Therefore, based on our field investigation, numerical simulation and previous studies, the long runout of the Tahman landslide is considered to be caused by its large volume coupled with its interaction with moraines.

Table 3 Back-analysis of peak ground acceleration (PGA) under different effective durations

| Effective duration (s) | Critical PGA (g) | Best-fitting PGA (g) |
|------------------------|------------------|----------------------|
| 15 | 0.63 | 0.86 |
| 25 | 0.6 | 0.77 |
| 35 | 0.56 | 0.76 |
| 45 | 0.54 | 0.74 |
| 55 | 0.53 | 0.72 |

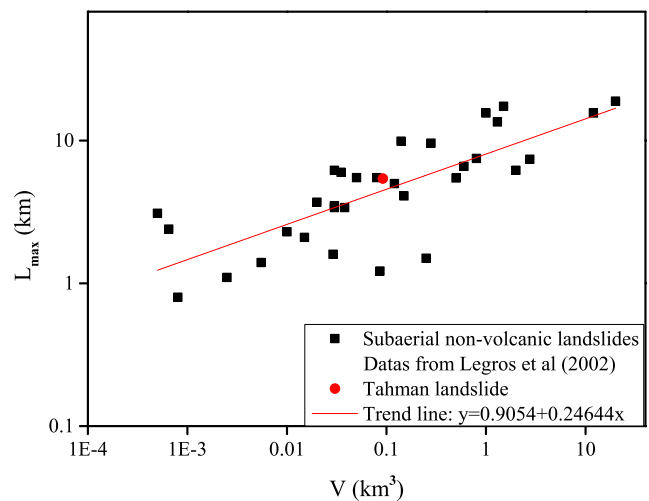
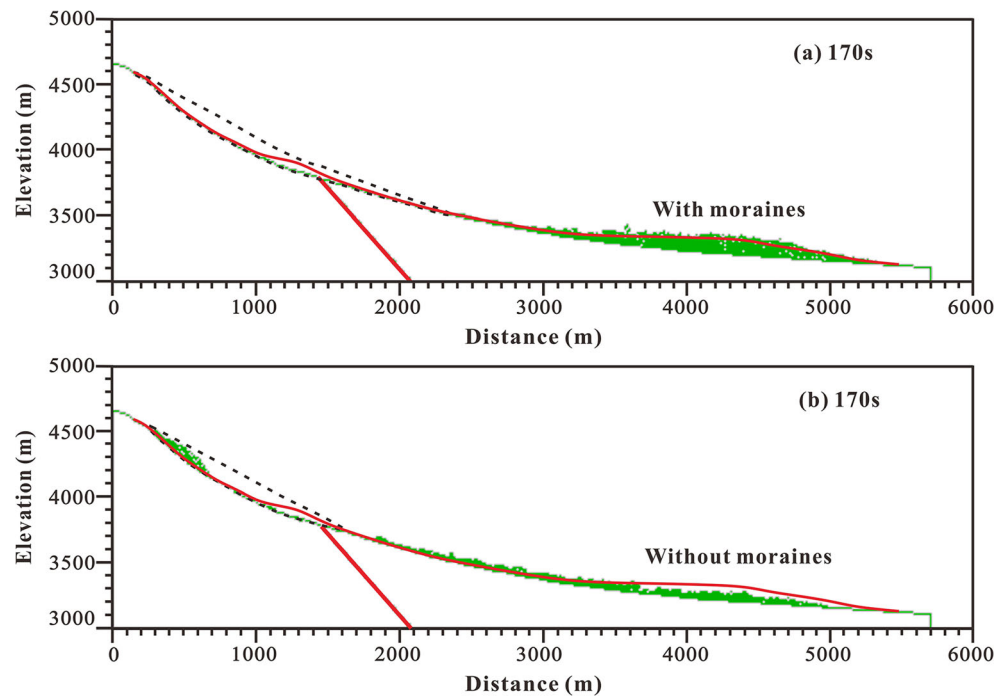


Fig. 13 Relationship between runout distance (L_{max}) and landslide volume (V) (after Legros et al. 2000)

Fig. 14 The influence of moraines on the runout distance of landslide debris: a with moraines; b without moraines



Conclusions

The present study provides a detailed investigation on the Tahman paleolandslide. The field survey showed it to be a large-scale rock avalanche with a volume of about $92 \times 10^6 \text{ m}^3$, with a vertical drop of 1500 m from EL 4800–3300 m, over a horizontal distance of 5420 m, and yielding a friction coefficient of about 0.28. Qualitative evidence relevant to earthquake seismic triggering was acquired by regional geological and tectonic backgrounds and the field investigation, which can provide some basis for quantitative numerical analyses. The conclusions drawn from the present study are as follows:

- (1) Under an average effective duration, landsliding occurred when PGA reached 0.55 g, which is suggested to be the critical PGA from triggering landslides. When the PGA increased to 0.76 g, the best-fitting result was obtained by calibrating the simulation results with the current geomorphological feature of the deposits. Although the accuracy of the PGA value may be limited by discrepancies between the natural seismic wave and sinusoidal wave used in our study, it is considered to be within an acceptable range.
- (2) The amplification of PGA in the Tahman rock slope was related to topography. According to the monitoring results from profiles S1–S7 and B1–B6, the horizontal PGA amplification coefficients tended to increase with elevation both on the surface of the slope and inside the slope, and the top of the slope was amplified the most. At

the same elevation, the PGA was amplified to a greater degree at the slope surface compared with inside the slope.

- (3) The effective duration of the seismic wave has a significant effect on the back-analyzed PGA value, which decreases with increasing effective duration.
- (4) The long runout of the Tahman landslide is mainly caused by its large volume and the interaction of the slide mass with moraines.

Acknowledgements This study was financially supported by the National Key R&D Program of China (project code 2018YFC1505001) and the National Natural Science Fund (grant number 41672359). The authors would like to thank the reviewers for their constructive comments, which improved the paper.

References

- Arnaud NO, Brunel M, Cantagrel JM, Tapponnier P (1993) High cooling and denudation rates at Kongur Shan, eastern Pamir (Xinjiang, China) revealed by $^{40}\text{Ar}/^{39}\text{Ar}$ alkali feldspar thermochronology. *Tectonics* 12(6):1335–1346
- Bhasin R, Kaynia AM (2004) Static and dynamic simulation of a 700-m high rock slope in western Norway. *Eng Geol* 71(3):213–226
- Bommer JJ, Martinez PA (1999) The effective duration of earthquake strong motion. *J Earthq Eng* 3(2):127–172
- Boulton N, Stead D, Schwab J, Geertsema M (2006) The Zymoetz River rock avalanche, June 2002, British Columbia, Canada. *Eng Geol* 83(1):76–93
- Brunel M, Arnaud N, Tapponnier P, Pan Y, Wang Y (1994) Kongur Shan normal fault: type example of mountain building assisted by extension (Karakoram fault, eastern Pamir). *Geology* 22(8):707–710

- Cao YB, Dai FC, Xu C, Tu XB, Min H, Cui FP (2011) Discrete element simulation of deformation and movement mechanism for Tangjiashan landslide. *Chin J Rock Mech Eng* 30(S1):2877–2887 (in Chinese with English Abstract)
- China Institute of Water Resources and Hydropower Research (1991) Manual of rock mechanics parameters. Water Resources and Electric Power Press, Beijing (in Chinese)
- Corominas J (1996) The angle of reach as a mobility index for small and large landslides. *Can Geotech J* 33(2):260–271
- Crozier MJ (1992) Determination of paleoseismicity from landslides. In: Bell DH (ed) *Landslides. Proceedings of the 6th international symposium, vol 2*. Balkema, Rotterdam, pp 1173–1180
- Dai FC, Lee CF, Ngai YY (2002) Landslide risk assessment and management: an overview. *Eng Geol* 64(1):65–87
- Dai FC, Tu XB, Xu C, Gong QM, Yao X (2011) Rock avalanches triggered by oblique-thrusting during the 12 May 2008 Ms 8.0 Wenchuan earthquake, China. *Geomorphology* 132(3):300–318
- Davies TRH (1982) Spreading of rock avalanche debris by mechanical fluidization. *Rock Mech* 15(1):9–24
- Evans SG, Mugnozza GS, Strom AL, Hermanns RL (2006) Landslides from massive rock slope failure and associated phenomena. Springer, Netherlands, pp 3–52
- Gaudio VD, Wasowski J (2011) Advances and problems in understanding the seismic response of potentially unstable slopes. *Eng Geol* 122(1):73–83
- GB 18306 (2015) Seismic ground motion parameters zonation map of China. China Standard Press, Beijing (in Chinese)
- Harp EL, Jibson RW (2002) Anomalous concentrations of seismically triggered rock falls in Pacoima canyon: are they caused by highly susceptible slopes or local amplification of seismic shaking? *Bull Seismol Soc Am* 92(8):3180–3189
- Havenith HB, Strom A, Jongmans D, Abdrakhmatov A, Delvaux D (2003a) Seismic triggering of landslides, part a: field evidence from the northern Tien Shan. *Nat Hazard Earth Syst Sci* 3(1/2):135–149
- Havenith HB, Strom A, Calvetti F, Jongmans D (2003b) Seismic triggering of landslides. Part B: simulation of dynamic failure processes. *Nat Hazards Earth Syst Sci* 3(6):663–682
- Hoek E, Brown ET (1997) Practical estimates of rock masses strength. *Int J Rock Mech Min Sci* 34(8):1165–1186
- Huang RQ (2009) Mechanism and geomechanical modes of landslide hazards triggered by Wenchuan 8.0 earthquakes. *Chin J Rock Mech Eng* 28(6):1239–1248 in Chinese with English Abstract
- Huang RQ, Li WL (2008) Research on development and distribution rules of geohazards induced by Wenchuan earthquake on 12th MAY, 2008. *Chin J Rock Mech Eng* 27(12):2585–2592 (in Chinese with English Abstract)
- Hungro O, Evans SG (2004) Entrainment of debris in rock avalanches: an analysis of a long run-out mechanism. *Geol Soc Am Bull* 116(9):1240–1252
- Hungro O, Morgenstern GC, Kellerhals R (1984) Quantitative analysis of debris torrent hazards for design of remedial measures. *Can Geotech J* 21(4):663–677
- Itasca (2004) UDEC: user's guide (version 4.0). Itasca Consulting Group, Inc., Minneapolis
- Jibson RW (1996) Use of landslides for paleoseismic analysis. *Eng Geol* 62(9):397–438
- Keefer DK (1984) Landslides caused by earthquakes. *Geol Soc Am Bull* 22(2):406–421
- Kveldsvik V, Kayni AM, Nadim F (2009) Dynamic distinct-element analysis of the 800 m high Aknes rock slope. *Int J Rock Mech Min Sci* 46(4):686–698
- Legros F, Cantagrel JM, Devouard B (2000) Pseudotachylite (frictionite) at the base of the Arequipa volcanic landslide deposit (Peru) and implications for emplacement mechanisms. *Geology* 108(5):601–611
- Lo CM, Lin ML, Tang CL, Hu JC (2011) A kinematic model of the Hsiaolin landslide calibrated to the morphology of the landslide deposit. *Eng Geol* 123(1–2):22–39
- Long W, Chen J, Wang PF (2015) Formation mechanism and back-analysis of paleoseismic parameters of the Temi large-scale ancient landslide in the upper Jinsha River. *J Seismol Res* 37(5):71–76 (in Chinese with English Abstract)
- Meunier P, Hovius N, Haines JA (2007) Regional patterns of earthquake-triggered landslides and their relation to ground motion. *Geophys Res Lett* 34:L20408
- Meunier P, Hovius N, Haines JA (2008) Topographic site effects and the location of earthquake induced landslides. *Earth Planet Sci Lett* 275(3):221–232
- Patar N, Mamatieri A, Guleti G, Zinati G (2016) Climate change feature analysis of Tashkurgan county from 1961 to 2015. *Desert Oasis Meteorol* 10(S1):80–90 (in Chinese)
- Robinson AC, Yin A, Manning CE, Harrison TM, Zhang SH (2004) Tectonic evolution of the northeastern Pamir: constraints from the northern portion of the Cenozoic Kongur Shan extensional system. *Geol Soc Am Bull* 116(7):953–974
- Robinson AC, Yin A, Manning CE, Harrison TM, Zhang SH, Wang XF (2007) Cenozoic tectonics of the NE Pamir, Western China, implication for the evaluation of the western end of the Indo Asian collision zone. *Geol Soc Am Bull* 119:882–896
- Scheidegger AE (1973) On the prediction of the reach and velocity of catastrophic landslides. *Rock Mech Rock Eng* 5(4):231–236
- Seong YB, Owen LA, Yi C, Finkel RC, Schoenbohm L (2009) Geomorphology of anomalously high glaciated mountains at the northwestern end of Tibet: Muztag Ata and Kongur Shan. *Geomorphology* 103(2):227–250
- Sonmez H, Ulusay R (1999) Modifications to the geological strength index (GSI) and their applicability to stability of slopes. *Int J Rock Mech Min Sci* 36(6):743–760
- Sun BG, Mao WY, Feng YR (2006) Study on the change of air temperature, precipitation and runoff volume in the Yarkant river basin. *Arid Zone Res* 23(2):203–209 (in Chinese with English Abstract)
- Tsou CY, Feng ZY, Chigira M (2011) Catastrophic landslide induced by typhoon Morakot, Shialin, Taiwan. *Geomorphology* 127(3):166–178
- Wechsler N, Katz O, Dray Y, Gonen I, Marco S (2009) Estimating location and size of historical earthquake by combining archaeology and geology in umm-El-Qanatir, Dead Sea transform. *Nat Hazards* 50(1):27–43
- Welkner D, Eberhardt E, Hermanns RL (2010) Hazard investigation of the Portillo rock avalanche site, Central Andes, Chile, using an integrated field mapping and numerical modelling approach. *Eng Geol* 114(3–4):278–297
- Wolter A, Gischig V, Stead D, Clague JJ (2016) Investigation of geomorphic and seismic effects on the 1959 Madison canyon, Montana, landslide using an integrated field, engineering geomorphology mapping, and numerical modelling approach. *Rock Mech Rock Eng* 49(6):2479–2501
- Yin YP, Wang FW, Sun P (2009) Landslide hazards triggered by the 2008 Wenchuan earthquake, Sichuan, China. *Landslides* 6(2):139–151
- Yuan GX, Shang YJ, Lin DM (2009) Engineering geological properties and stability analysis of moraine debris slopes in Palong River drainage area along Sichuan-Tibet highway. *Eng Geol* 17(2):188–194
- Yuan ZD, Chen J, Li WQ (2012) ¹⁰Be dating of Taheman large scale landslide in eastern Pamir and paleoseismic implications. *Quat Sci* 32(3):409–416 (in Chinese with English Abstract)
- Zhou JW, Cui P, Yang XG (2013) Dynamic process analysis for the initiation and movement of the Donghekou landslide-debris flow triggered by the Wenchuan earthquake. *J Asian Earth Sci* 76(S1):70–84